J. Phys. Chem. A **2004,** *108,* 5365−5376

Infrared Optical Constants for Carvone from the Mie Inversion of Aerosol Extinction Spectra

Michelle T. Dohm, Allison M. Potscavage, and Richard F. Niedziela*

Department of Chemistry, DePaul University, Chicago, Illinois 60614-3251

Received: August 27, 2003; In Final Form: April 8, 2004

Frequency-dependent, complex refractive indices for carvone in the mid-infrared from 750 to 5000 cm^{-1} have been inverted from the Fourier transform extinction spectra of laboratory-generated aerosols recorded at room temperature. The refractive indices obtained in this analysis are in good qualitative agreement with the results of a previous thin-film study of carvone. However, a full quantitative assessment of this agreement cannot be made as tabulated data for the previous study are no longer available. The refractive indices, or optical constants, reported here add to the small number of frequency-dependent refractive index data sets for other organic compounds that are available in the literature. Such data can be used to elucidate the optical properties of a substance, which are of critical importance in the interpretation of remote sensing data and in the evaluation of how atmospheric particulate matter consisting of organic compounds may affect climate change.

1. Introduction

Aerosols are now recognized as having a potentially significant impact on the environment with regard to human health, ozone depletion, urban smog, visibility, and climate change on both local and global levels. The absolute environmental impact of these small particles cannot be fully evaluated at this time due to incomplete knowledge about their chemical, optical, and physical properties[1] as well as their complex spatial and temporal distributions throughout the atmosphere.[2] Nowhere is the lack of information on aerosol properties more obvious than in the troposphere. The term tropospheric aerosol alone covers five different classifications of particles including soil dust, sulfates, sea salt, soot, and organic aerosols; of these, only sulfate particles have been characterized to any extent.[3] Organic aerosols are, however, the least understood although they contribute greatly to the amount of particulate matter in industrialized and urban areas[4] and play roles in a variety of natural phenomena such as haze formation in nonurban settings.[5,6] Since many different anthropogenic and biogenic sources inject organic compounds into the troposphere, the composition of organic aerosols and their modes of formation can vary a great deal and depend heavily on a number of parameters including geographic location, season, weather, and time of day. For example, primary organic aerosols (POAs) are emitted directly into the troposphere by some mechanical means such as the wind abrasion of plant leaves[7,8] or the breaking of waves on bodies of water.[9] As such, POAs tend to be in the form of oil droplets or waxy solids made from high molecular weight compounds. They typically are present in small numbers and have effective diameters greater than 1 μm, which cause them to quickly settle out of the atmosphere. Secondary organic aerosols (SOAs), on the other hand, are formed when low vapor pressure, gas-phase products of organic oxidation reactions either undergo homogeneous nucleation or condense onto preexisting particles.[10−12] Unlike POAs, SOAs have diameters less than 1 μm, higher number densities, and lifetimes that can span days.

As with inorganic particles and gas-phase molecules, organic aerosols principally interact with solar (short-wave) and terrestrial (long-wave) electromagnetic radiation. During this interaction, photons may be absorbed and converted into other forms of internal energy within the aerosol or scattered into directions other than their incoming trajectories. Together, these two processes contribute to the extinction of light by the aerosol and have the potential to directly affect climate by altering the amount of light passing through the troposphere.[2,13] For instance, particles tend to become more efficient at scattering photons whose wavelengths are comparable to the diameters of the particles. Small organic aerosols, like SOAs, are therefore thought to be able to scatter short-wave radiation back into space, thus providing a cooling component to the climate. Organic compounds also often have a rich manifold of absorption bands in the mid-infrared due to molecular vibrational modes. Aerosols consisting of organic materials, particularly those with bands in the atmospheric window between 8 and 12 μm, may act like greenhouse gases by absorbing and reemitting infrared radiation. In this manner, organic aerosols may make a small contribution to climate warming.[14] Consequently, a full assessment of the direct effect of organic particles on climate hinges on how well their ability to absorb and scatter light can be characterized.[15] Such optical characterization is also important in the interpretation of data collected in remote sensing applications designed to probe the properties of naturally occurring aerosols.[16]

The extinction of light by an aerosol is not only dependent on particle size but particle shape and number density as well. It also depends on the frequency of the light, $\tilde{\nu}$ (expressed here in units of wavenumber, cm^{-1}), through the complex refractive indices, N, of the material from which the aerosol is made. Here N is defined as

$$N(\tilde{\nu}) = n(\tilde{\nu}) + ik(\tilde{\nu}) \tag{1}$$

where n and k are the real and imaginary components of the complex refractive indices, respectively. The latter determines

---

* Corresponding author. E-mail: rniedzie@condor.depaul.edu

10.1021/jp0365559 CCC: $27.50

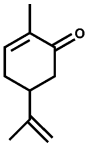

Figure 1. Two-dimensional representation of the molecular structure of carvone.

the absorption characteristics of the material while the former is responsible for photon redirection within the substance. When used with an appropriate optical model such as Mie scattering theory for spherical particles, the complex refractive indices, or optical constants, as they are also referred to, may be used to reveal the optical properties of an aerosol.[17−19] Despite the availability of many reference spectra, however, very little refractive index data for organic compounds appear to have been reported in the literature.[15] Indeed, a recent search yielded infrared optical constants for only benzene,[20,21] chlorobenzene,[22] chloroform,[21] toluene,[23] dichloromethane,[24] methanol,[25] products of vegetation burning,[26] several terpenes and polycyclic aromatic hydrocarbons (PAHs),[27] and most recently, dihydroxyacetone.[28] In addition to this lack of primary optical data, a more thorough understanding of how best to use the complex refractive indices of pure compounds to model optical properties of actual particles is needed. As previously mentioned, organic aerosols are likely to be composed of many different components and their overall optical characteristics will undoubtedly be influenced by the mixing state of their constituent materials.[29] Many questions still remain as to how optical constants of pure components should be "mixed" to best optically describe actual particles found in the atmosphere.[17,29−31]

In this paper, we report the infrared (IR), frequency-dependent complex refractive indices for carvone at 25 °C. The refractive indices were obtained from a Mie inversion of aerosol extinction spectra using a procedure that is based on a method previously reported in detail by Clapp et al.[32] and has been used elsewhere to determine the optical constants of other materials with atmospheric relevance.[33−36] It has been suggested that optical data from such laboratory-based aerosol observations may better represent actual atmospheric particulate matter than those from bulk or thin-film studies, especially when interactions at the material/substrate interface are possible.[37] As for the particular molecule studied here, carvone ($C_{10}H_{14}O$, see also Figure 1) belongs to a class of compounds known as monoterpenes, which are naturally occurring materials that are biosynthesized in plants. Monoterpenes are principally characterized by their carbon content (C_{10}), come in a variety of cyclic and acyclic structures, and typically contain at least one unsaturated site.[38] Once emitted into the troposphere, monoterpenes can be oxidized by species such as O_3, HO, and NO_3, thus making them active participants in tropospheric chemistry. Carvone itself is an α,β-unsaturated ketone and is found in many essential oils including those of dill, caraway, and spearmint.[39] Although carvone is not emitted at a rate comparable to other monoterpenes such as α- and β-pinene, its structure nonetheless gives rise to spectroscopic features that are representative of materials that might be found in actual organic aerosols. One particularly important structural feature of carvone is the carbonyl functional group that is present in aldehydes and ketones, two types of products formed as a result of the gas-phase oxidation of organic molecules.[4,40] The present complex refractive indices will be qualitatively compared to those of Sutherland et al. (SKO)[27] which were obtained by inverting thin-film transmission measurements. Unfortunately, a full quantitative comparison cannot be made since the SKO data set is no longer available in tabulated form.[41]

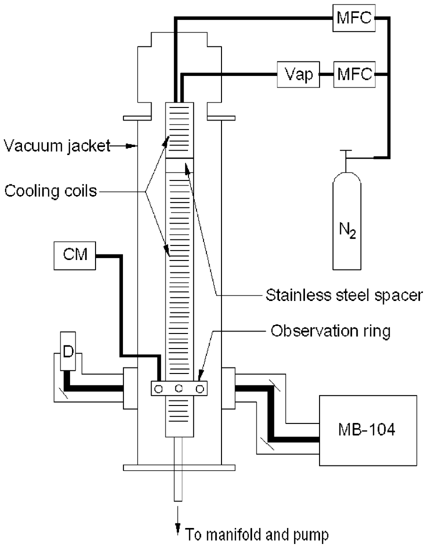

Figure 2. Schematic diagram of the aerosol flow cell. The cell is made from three sections of copper tubing, each of which is temperature-controlled by a recirculating chiller. Carvone aerosols are injected at the top of the cell and eventually flow through the observation ring where they are probed by the beam from the FT-IR spectrometer. In this diagram, MFC represents a mass flow controller, Vap the aerosol vaporizer source, and CM the capacitance manometer.

2. Experiment

2.1. Aerosol Flow Cell. Carvone aerosols were studied in a newly constructed laminar flow cell that consists of three sections of 7.72 cm diameter copper tubing as shown schematically in Figure 2. The top section is 20 cm long and is separated from the 105 cm long middle section by a 5 cm long, thin-walled stainless steel spacer. The bottom section has a length of 10 cm and is connected to the middle section by a 5 cm thick observation ring. The ring was machined from solid brass and contains six equally spaced radial ports through which the aerosol stream may be observed. Of these, two ports are enclosed by 25 mm diameter Cleartran windows (Janos Technologies) through which the spectrometer beam passes. Two other ports are sealed by 25 mm diameter borosilicate glass windows and allow the aerosol stream to be visually inspected. Finally, one of the two remaining ports houses a sampling probe for a MKS 390HA capacitance manometer that is used to monitor the cell pressure. Each port is offset from the main aerosol flow by 3 cm to avoid contamination of the windows via deposition. All seals between the windows and observation ring, as well as seals between the sections of the flow cell, are made from indium wire.

The temperature of the top section was regulated by flowing 50% (v/v) ethylene glycol from a recirculating chiller through a copper coil that is soldered to the cell wall. Coils for the middle and bottom sections, along with the observation ring, are connected in series to a separate chiller and are regulated in the same fashion. While the stainless steel spacer between the top section and the remainder of the cell permits the top of the cell to be independently temperature-controlled, in these experiments, all sections were maintained at a temperature of 298 ± 1 K as measured by an array of six strategically spaced platinum resistance thermometer sensors (RTDs, Minco Products, Inc.). To minimize temperature fluctuations due to contact with the

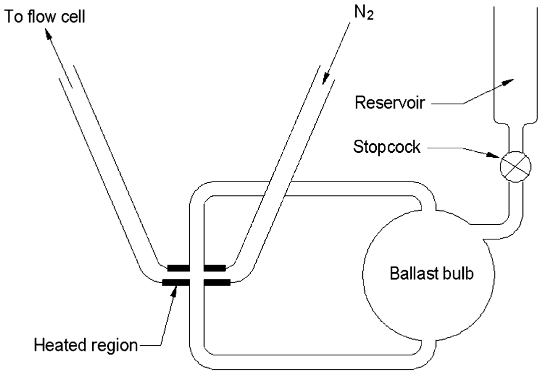

Figure 3. Schematic diagram of the vaporizer used in this study. The vaporizer is constructed from borosilicate glass. Heat is applied to the bottom of the vaporizer through a piece of resistive heat tape wrapped around the tube.

atmosphere, the entire flow cell assembly is enclosed in an acrylic vacuum jacket.

2.2. Aerosol Generation. Carvone aerosols were produced via homogeneous nucleation in a glass vaporizer (Figure 3). The vaporizer is similar to that used by Lovejoy et al.[42] in their work with sulfuric acid aerosols. In the present case, however, a filling reservoir and ballast bulb were added to facilitate the online replenishment of carvone. Briefly, (*R*)-(−)-carvone (Aldrich, 98%, used without further purification) was placed into the source reservoir and allowed to flow into the vaporizer and ballast bulb until each was half full. The bottom of the vaporizer was heated to increase the local vapor pressure of carvone. A regulated stream of nitrogen (99.998%) established by a mass flow controller (MKS 1179A) with flow rates up to 10 standard liters per minute (slm) was then allowed to pass through the vaporizer, sweeping carvone vapor out of the heated region into the relatively cooler output arm of the vaporizer. Here, the vapor became supersaturated and the formation of carvone aerosol ensued. The particles remained in the nitrogen stream and were subsequently injected through one of five ports at the top of the flow cell. An additional mass flow controller was available to admit nitrogen into the cell through one of the other injection ports to change the overall flow, if needed. The contents of the cell were removed from the bottom section by a cryotrapped mechanical pump (Edwards RV-12). A manifold of metering needle valves was used to throttle the flow out of the cell and, when coupled with the mass flow controller settings, established the desired steady state pressure in the cell during each run. The median particle size produced by the vaporizer is primarily a function of pressure, flow rate, and temperature. In general, the production of large particles with radii much greater than 1 μm was favored under conditions of high pressure, high vaporizer temperature, and low flow rate. Small particles with radii less than 1 μm, on the other hand, were preferably formed under conditions of lower pressure and higher flow rate.

2.3. Extinction Spectra. Aerosol extinction spectra were recorded over a range from 700 to 5000 cm^{-1} by a Bomem MB-104 benchtop Fourier transform infrared (FT-IR) spectrometer. The optical path from the spectrometer to the detector was evacuated through the vacuum jacket surrounding the flow cell while the spectrometer itself was purged with flowing nitrogen (Figure 2). More specifically, the infrared beam emitted from the side port of the spectrometer was directed through the flow cell by a pair of 90° off-axis paraboloid (OAP) mirrors that also reduced the beam diameter by a factor of 2 in order to pass through the cell windows. Afterward, the beam was intercepted by another 90° OAP that focused the infrared light onto a 1 mm^2 mercury−cadmium−telluride (MCT) detector (EG&G J15D22-M205-S01M-60). The detector signal was amplified 1000 times (EG&G PA-101) before being sent into the spectrometer's data acquisition interface. The aerosol extinction spectra used in this study represent the co-addition of twenty interferograms, each recorded with a resolution of 2 cm^{-1} and referenced against a background spectrum that was taken with nitrogen flowing through the cell just prior to starting up the aerosol source. Empty cell spectra were taken periodically to ensure that materials were not deposited on the flow cell windows that would otherwise affect the recording of aerosol extinction spectra. To avoid potential photometric errors due to nonlinear behavior in the MCT detector at high absorbance values, we took care to use only those spectra whose absorption band heights were near 0.8 or below. Richardson et al.[43] note that most spectrometers that utilize MCT detectors behave linearly over this range. We found this to be true in the case of the present system based on unrelated calibration studies involving gas-phase absorption measurements.[44]

Thin-film spectra of carvone were recorded using the sampling region on top of the FT-IR spectrometer. In this case, background spectra were recorded by placing two KBr disks back-to-back in a mount at the focus of the infrared beam. A small drop of carvone was then placed on the top edge between the disks and allowed to wick between them. The attenuation of the infrared beam was measured by a room-temperature DTGS detector over a range from 700 to 5000 cm^{-1} at a resolution of 2 cm^{-1}. As with all aerosol extinction spectra, the thin-film spectra represent the co-addition of twenty interferograms. The KBr disks used in the thin-film measurements were purposely not clamped together in order to minimize, but not completely eliminate, the appearance of sinusoidal interference spectra which usually appear in systems with optically flat, parallel plates. When weak interference spectra were observed in the thin-film baseline at high wavenumber, they were removed by subtracting the results of a nonlinear, least-squares sinusoidal fit of the extinction data in this region from the observed thin-film spectrum.

Carvone spectra in the visible and ultraviolet (UV) regions of the electromagnetic spectrum were recorded from 12000 to 50000 cm^{-1} on a Cary/1 UV−visible spectrometer using matched quartz cells and spectroscopy grade cyclohexane (Aldrich) as the solvent.

2.4. Temperature-Dependent Measurements of n_D. The temperature dependence of the real refractive index at the sodium D-line (589.3 nm), n_D, for carvone was measured to within ± 0.0001 using an Abbe refractometer (Bausch & Lomb). Temperature control of the refractometer was achieved by flowing 50% (v/v) ethylene glycol from a recirculating chiller through both prism mounts. All temperatures were recorded at the fluid outlet with an RTD to ± 0.01 K.

3. Mie Inversion Procedure

3.1. Background. Inversion methods are routinely used to extract fundamental properties of matter that cannot be obtained directly from experimental measurements. Such is the case for complex refractive indices, which are usually retrieved from measurements of reflectivity, angular scattering, or extinction with the aid of a suitable optical model.[17] Aerosol extinction spectra, *E*, are readily obtained in the laboratory or field (e.g., satellite observations) by measuring the frequency-dependent attenuation in the irradiance, *I*, of a beam of light as it passes through an ensemble of particles. After accounting for attenuation due to gas-phase species, the observed reduction in irradiance is due to the absorption and scattering of photons by the particles, as shown in the Beer−Lambert law of extinction

$$E(\tilde{\nu}) = -\ln(I(\tilde{\nu})/I_0(\tilde{\nu})) = (\alpha_{\mathrm{abs}}(\tilde{\nu}) + \alpha_{\mathrm{sca}}(\tilde{\nu}))L \qquad (2)$$

where I_0 is the irradiance of the beam incident upon the aerosol, α_{abs} and α_{sca} are, respectively, the volume coefficients of absorption and scattering, and L is the path length through the aerosol. Mie scattering theory is the natural optical model of choice to use in inverting aerosol extinction spectra, especially when the particles under study are, or are approximately, spherical and their diameters are comparable to the wavelength of light. Mie theory provides the connection between the volume coefficients in eq 2, the geometry of the particles, and the optical constants of the material, or materials, that the aerosol is made from. Indeed, Mie calculations are frequently performed to compute the absorption and scattering characteristics of aerosols for which particle sizes and refractive index data are available. However, the use of Mie theory in the retrieval of complex refractive indices from extinction spectra is not as straightforward and can yield results that are not unique unless the inversion procedure is properly constrained.[45] One such constraint is the use of particle size distribution to weight the computed extinction components. The distribution can be independently measured[28,45] or assumed to have a functional form.[32] In either case, a log-normal distribution function,

$$P_{\mathrm{LN}}(r;r_{\mathrm{g}},\sigma_{\mathrm{g}}) = \frac{1}{\sqrt{2\pi}r\ln\sigma_{\mathrm{g}}}\exp\left[-\frac{1}{2}\left(\frac{\ln(r/r_{\mathrm{g}})}{\ln\sigma_{\mathrm{g}}}\right)^2\right] \qquad (3)$$

is typically used to represent a range of aerosol sizes where r is the particle radius, r_{g} is the geometric mean (or median) radius, and σ_{g} is the geometric mean standard deviation.[18] This function has been shown to yield good empirical fits to measured size distributions for many natural and laboratory-generated aerosols.[46] Another constraint that is placed on Mie inversions comes in the form of the Kramers−Kronig (KK) dispersion relationship between the refractive index components n and k

$$n(\tilde{\nu}_i) = n(\infty) + \frac{2}{\pi}P\int_0^{\infty}\frac{\tilde{\nu}k(\tilde{\nu})}{(\tilde{\nu}^2 - \tilde{\nu}_i^2)}d\tilde{\nu} \qquad (4)$$

which shows that n at any particular frequency $\tilde{\nu}_i$ depends on $n(\infty)$, the real component at infinite frequency, and the integral over the imaginary components of the complex refractive indices at all frequencies, where P indicates that the Cauchy principal value is to be taken.[47]

Inversion methods are typically classified as either analytical or empirical, depending on the techniques used in inverting the experimental data.[48] Most Mie inversions fall under the latter classification due to their use of iterative procedures in which the parameters of the optical model, or the optical constant data itself, are varied until the deviations between the Mie spectrum predicted by the optical model and an observed extinction spectrum are minimized.[49] For example, studies done by Milham et al.[45] and more recently by Signorell and Luckhaus[28] employ procedures in which k is numerically adjusted at each frequency, followed by the recalculation of n via the subtractive KK relationship,[50,51] until the Mie scattering spectrum computed from these data best fit an experimental spectrum for an aerosol whose size distribution was independently measured. Clapp et al.[32] (see also refs 33−36) devised a Mie inversion method for cases in which the particle size distribution is not, or simply cannot be, easily measured. In that method, they assumed their particle sizes to be distributed log-normally per eq 3 and admitted r_{g} and σ_{g} as variable parameters in their procedure. In addition, they initiated their Mie inversion with an estimate of the frequency dependence of k by exploiting the relationship between the imaginary component and the absorption coefficient

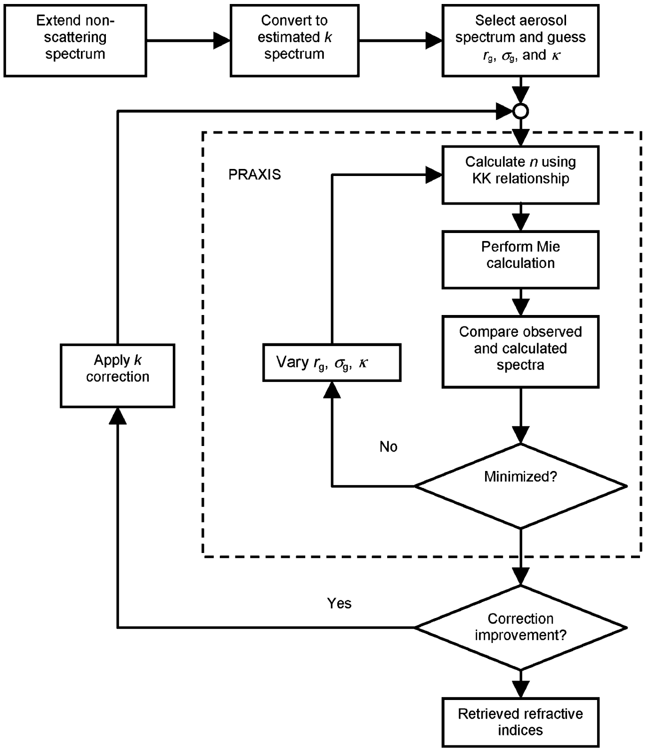

Figure 4. This flowchart depicts the general logic flow of the inversion procedure. The dashed box encloses those operations that are carried out within each PRAXIS minimization.

$$k = \alpha_{\mathrm{abs}}/4\pi\tilde{\nu} \qquad (5)$$

for a "nonscattering" aerosol extinction spectrum. Since $\alpha_{\mathrm{abs}} \gg \alpha_{\mathrm{sca}}$ for such spectra, they assumed that k was directly related to $E/\tilde{\nu}$ via eq 2 and introduced a third parameter to act as a proportionality coefficient that principally accounts for the fact that the path length through the aerosol used in their study was not accurately known. This set of imaginary components was then used in a subtractive KK calculation to determine n. All three parameters were varied in a nonlinear, iterative least-squares routine until the best possible agreement between the computed and an observed aerosol extinction spectrum was achieved. While the fits of Clapp et al.[32] generally showed good agreement overall at the end of this iterative process, some spectral mismatches did occur at the local band level. These mismatches were ultimately due to the assumption of linear proportionality between k and $E/\tilde{\nu}$ which, strictly speaking, is only valid for bulk measurements in cases where the detector is optically identical to the surrounding media.[17] Reflections off of windows or other materials along the optical path also contribute to observed extinction measurements in a manner that is not directly related to absorption by the material under study.[29] In reality, therefore, the proportionality coefficient described above is a weak function of frequency, a fact that was corrected for in different ways by Clapp et al.[32] and the other studies that have used their inversion method.[33−36]

3.2. Initiation. The current inversion procedure, summarized by the flowchart in Figure 4, closely follows the method

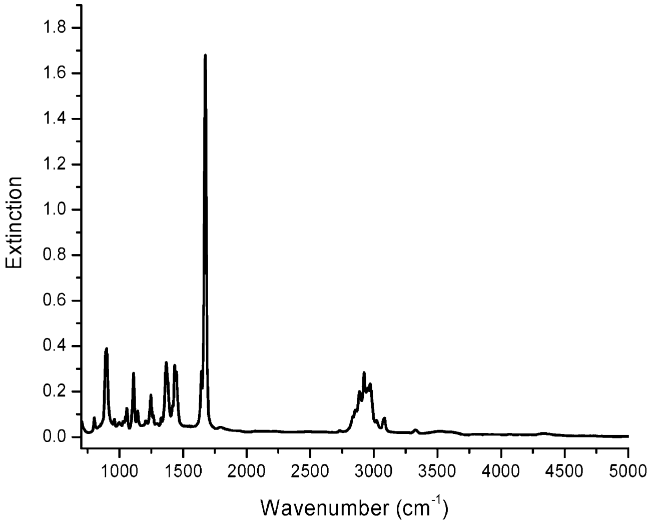

Figure 5. Thin-film carvone spectrum that was used to estimate k at the outset of each inversion.

established by Clapp et al.[32] In this study, however, we explored the possibility of using a thin-film instead of a nonscattering aerosol extinction spectrum to obtain an estimate of the frequency dependence of k throughout the mid-infrared since it too is dominated by absorption. Indeed, thin-film spectra have been used to provide "apparent" imaginary values in other optical constant retrieval methods[27,51,52] and in fact, this may be more convenient to measure depending on the conditions under which the material is being studied. The thin-film spectrum shown in Figure 5 was used to provide a set of scalable imaginary components by substituting the Beer–Lambert law for an extinction spectrum in which $\alpha_{\mathrm{sca}} \cong 0$ into eq 5 to obtain

$$k(\tilde{\nu}) = E(\tilde{\nu})/4\pi L\tilde{\nu} = \kappa k'(\tilde{\nu}) \qquad (6)$$

where $k' = (E/\tilde{\nu})/(E/\tilde{\nu})_{\max}$ is a unitless imaginary component template spectrum whose maximum value is set to unity, $(E/\tilde{\nu})_{\max}$ is the maximum value of $(E/\tilde{\nu})$ in the experimental thin-film spectrum, and $\kappa = (E/\tilde{\nu})_{\max}/4\pi L$ is a unitless scaling parameter that will be used in the current iterative inversion procedure to account for the fact that the thickness of the carvone film is not accurately known. This parameter also happens to conveniently represent the maximum value of the imaginary components and will be used later as a check on the precision of the method. Once the imaginary component template spectrum is created, the original thin-film spectrum is no longer referred to in the inversion procedure.

Before converting the thin-film data to a k spectrum via eq 6, it must be noted that the transmission characteristics of optical components, detector efficiency over the electromagnetic spectrum, and other instrumental limitations necessarily restrict extinction measurements to spectral windows and, as a result, the integral in the KK dispersion relationship (eq 4) cannot be fully evaluated. It is well-known that the truncation of this integral can lead to errors in n at either end of the frequency range, hence it is important to understand the impact of the imaginary parts of the complex refractive index in regions outside the experimental frequency range on the calculation of the real parts within.[16,35,53,54] The KK integral may be separated into three parts (see eq 7) where $\tilde{\nu}_{\mathrm{l}}$ and $\tilde{\nu}_{\mathrm{h}}$ indicate the low and high wavenumber limits of the experimental frequency range, respectively, and $\tilde{\nu}_{\mathrm{l}} \le \tilde{\nu}_i \le \tilde{\nu}_{\mathrm{h}}$. The denominators in the integrals of eq 7 cause the value of $n(\tilde{\nu}_i)$ to be most affected by imaginary components in the immediate vicinity of $\tilde{\nu}_i$; therefore, as $\tilde{\nu}_i$ approaches $\tilde{\nu}_{\mathrm{l}}$ or $\tilde{\nu}_{\mathrm{h}}$, n becomes more dependent on values of k just outside the experimental frequency range. This is not a problem if the imaginary components in the outer regions are exactly equal to zero. In the case of carvone and most other organic substances, however, this is not necessarily true. Rotational and vibrational modes give rise to nonzero imaginary components for $\tilde{\nu} < \tilde{\nu}_{\mathrm{l}}$ as do electronic transitions for $\tilde{\nu} > \tilde{\nu}_{\mathrm{h}}$. Since the low-frequency integral in eq 7 is inherently negative, ignoring its contribution causes a positive deviation in $n(\tilde{\nu})$ near $\tilde{\nu}_{\mathrm{l}}$ while ignoring the high-frequency integral has the opposite effect on the real part of the complex refractive indices near $\tilde{\nu}_{\mathrm{h}}$.

To minimize the deviation in n at low wavenumber, the k spectrum is usually extended past the low-frequency cutoff through one of several different techniques. This operation in effect admits additional imaginary components for consideration in the low-frequency integral and hence reduces the truncation error in the real component at $\tilde{\nu}_{\mathrm{l}}$. One such extension technique involves making an assumption about the behavior of k past the low-frequency cutoff. For example, in their work on sulfuric acid refractive indices, Tisdale et al.[54] set the imaginary components below 500 cm^{-1} equal to the value of k at 500 cm^{-1}, the lowest frequency in their data set. Biermann et al.,[53] on the other hand, assumed that k monotonically decreased to zero at 0 cm^{-1} from the end of their sulfuric acid data sets at 500 cm^{-1}. Alternatively, low-frequency data from other studies may be grafted onto experimental measurements as Niedziela et al. did in their optical constant retrievals for nitric acid dihydrate[34] and sulfuric acid.[35] While these methods reduce the errors in n at the low-frequency cutoff, care must be taken in how and when they are applied. As Lund Myhre et al.[16] point out, the magnitude of the optical constants may still be significantly affected if the extension method does not take large values of k into account for materials that have strong absorption features in the far-IR.

Our approach in this study is similar to the extension method utilized by Niedziela et al.[35] In the case of carvone, imaginary components at frequencies below the end of our data set at 700 cm^{-1} were not experimentally available. Instead, we digitized a reference extinction spectrum[55] of carvone between 450 and 700 cm^{-1} and scaled it to match the experimental thin film at 700 cm^{-1}. This working data set was then expanded to include experimental extinction data through 750 cm^{-1}. A cubic spline interpolation[56] of the expanded set was then performed to extend the thin-film extinction spectrum to 450 cm^{-1} at the frequency interval of the experimental spectrum before its use in eq 6. An expanded view of the result of this extension operation is shown in Figure 6.

The high-frequency integral in eq 7 covers, for all practical purposes, frequencies in the near-IR, visible, and ultraviolet regions of the electromagnetic spectrum. The imaginary components are expected to be quite small throughout the near-IR and visible regions for colorless compounds such as carvone, thus their contribution to n near $\tilde{\nu}_{\mathrm{h}}$ can be neglected. This is

$$n(\tilde{\nu}_i) = n(\infty) + \underbrace{\frac{2}{\pi}\int_0^{\tilde{\nu}_{\mathrm{l}}} \frac{\tilde{\nu}k(\tilde{\nu})}{(\tilde{\nu}^2 - \tilde{\nu}_i^2)}\, d\tilde{\nu}}_{\text{low}} + \underbrace{\frac{2}{\pi}\int_{\tilde{\nu}_{\mathrm{l}}}^{\tilde{\nu}_{\mathrm{h}}} \frac{\tilde{\nu}k(\tilde{\nu})}{(\tilde{\nu}^2 - \tilde{\nu}_i^2)}\, d\tilde{\nu}}_{\text{experimental}} + \underbrace{\frac{2}{\pi}\int_{\tilde{\nu}_{\mathrm{h}}}^{\infty} \frac{\tilde{\nu}k(\tilde{\nu})}{(\tilde{\nu}^2 - \tilde{\nu}_i^2)}\, d\tilde{\nu}}_{\text{high}} \qquad (7)$$

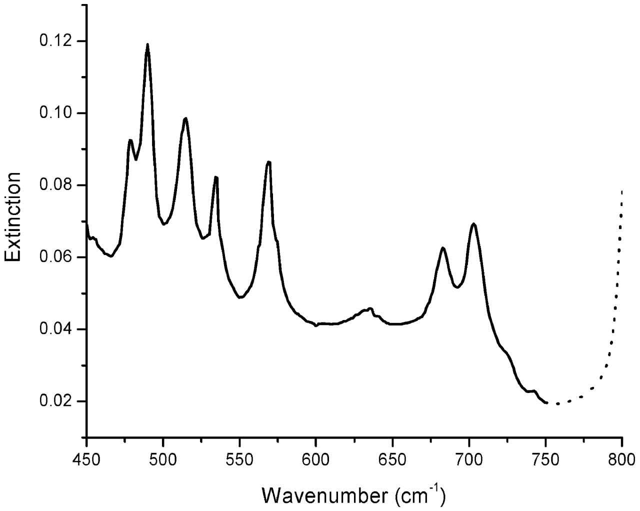

Figure 6. Detail of the extension to the thin-film spectrum. The solid line represents the spline interpolation of the digitized reference spectrum and the experimental spectrum between 700 and 750 cm^{-1}. The dashed line shows the original thin-film spectrum.

indeed verified by the lack of extinction in the UV−visible spectrum of carvone up to 25000 cm^{-1} (Figure 7). Two bands appear in the UV near 30000 cm^{-1} (333 nm) and 44000 cm^{-1} (227 nm), both of which are consistent with red-shifted $n\rightarrow\pi^*$ and $\pi\rightarrow\pi^*$ transitions, respectively, in the carbonyl chromophore of α,β-unsaturated ketones. The molar extinction coefficient for the first band is on the order of 10^1 L mol^{-1} cm^{-1}, while that of the second is 10^4 L mol^{-1} cm^{-1}. These values imply that the imaginary components in the UV are most certainly not equal to zero. Their contribution to n near $\tilde{\nu}_h$ though is mitigated by the fact that $\tilde{\nu} \gg \tilde{\nu}_h$. Since the overall impact of the high-frequency integral in eq 7 is expected to be small at best, we have taken k to equal to zero at all frequencies above 5000 cm^{-1}, the end of our experimental data set.

3.3. Kramers−Kronig Calculation. Several different numeric methods can be used to evaluate the KK integral in eq 4, each of which, in its own way, addresses the imbedded pole and the fact that the imaginary components are discrete, digitized sets of data.[47,57,58] Here we use a method based on Maclaurin's formula as presented by Ohta and Ishida[58] to calculate n. The method requires k to be equally spaced and is particularly appealing because its simplicity minimizes computation time and it avoids the use of approximations around the pole. In this case, the real component at a particular frequency is given by

$$n(\tilde{\nu}_i) = n(\infty) + \frac{2(\Delta\tilde{\nu})}{\pi}\sum_j{}' k(\tilde{\nu}_j)\left\{\frac{1}{\tilde{\nu}_j - \tilde{\nu}_i} + \frac{1}{\tilde{\nu}_j + \tilde{\nu}_i}\right\} \quad (8)$$

where $\Delta\tilde{\nu}$ is the spacing between successive data points, Σ' indicates that every other data point is included in the summation, and the starting value for index j depends on the value of i: when i is odd, $j = 2,4,6,...$, otherwise for even i, $j = 1,3,5,...$. In the present study, n is always calculated for all frequencies from 450 to 5000 cm^{-1}.

The only term in eq 8 that has not been addressed up to this point is $n(\infty)$, the value of the real component at infinite frequency. For colorless materials, it is customary to set $n(\infty)$ equal to the value of the real component at some frequency in the visible region that is far enough away from both IR and UV absorption bands.[59] A convenient value is n_D, the real component at the sodium-D line (16965 cm^{-1} or 589.3 nm) that is usually tabulated for most materials at 20 °C. The real component is sensitive to changes in density and is therefore implicitly dependent on temperature. We measured the temperature dependence of n_D for carvone as described above in order to interpolate its value at 25 °C for these experiments. The data, shown in Figure 8, were treated to a linear-regression and yielded a temperature coefficient, dn_D/dT, of (-4.28 ± 0.03) $\times$ 10^{-4} K^{-1}, a value consistent with most organic liquids.[60] Based upon these results, $n(\infty)$ was set to 1.497 ± 0.001 in all KK calculations.

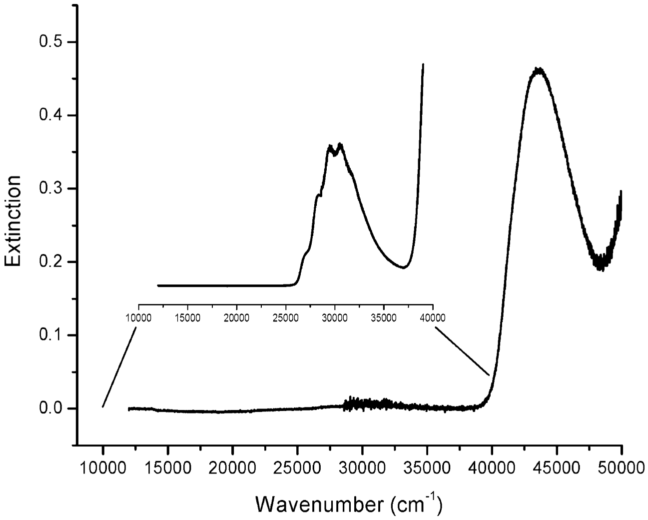

Figure 7. UV−visible spectrum of carvone (in cyclohexane) from 12000 to 50000 cm^{-1}. The inset spectrum shows the detail of the region up to 40000 cm^{-1}.

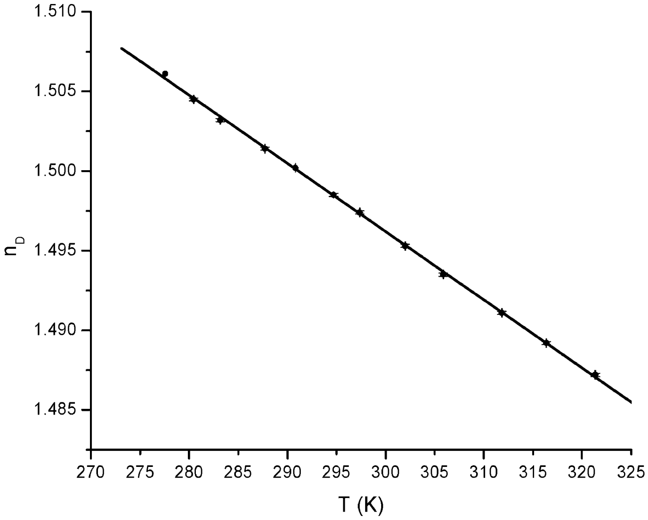

Figure 8. Plot of n_D versus temperature. The linear fit yielded a temperature dependence of $n_D = (1.6247 \pm 0.0009) - (4.28 \pm 0.03) \times 10^{-4}$ K^{-1} T, which in turn was used to interpolate n_D at 25 °C.

3.4. Mie Scattering Calculations. Mie scattering calculations were carried out using a modified form of Bohren and Huffman's BHMIE routine which calculates extinction and scattering efficiencies for a spherical particle of size parameter $x = 2\pi r\tilde{\nu}$ that is made from material having optical constants $n(\tilde{\nu})$ and $k(\tilde{\nu})$.[17] The efficiencies are used to calculate frequency-dependent, average extinction and scattering cross-sections weighted by the log-normal distribution function via

$$\langle C_{ext}(\tilde{\nu})\rangle = \sum_{r = r_g/\sigma_g^3}^{r_g\sigma_g^3} P_{LN}(r;r_g,\sigma_g)\pi r^2\, Q_{ext}(x(\tilde{\nu}),n(\tilde{\nu}),k(\tilde{\nu}))\Delta r \quad (9)$$

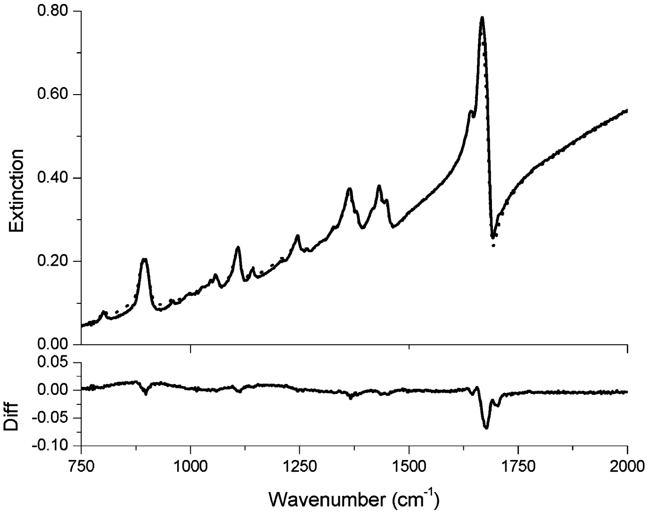

Figure 9. The top panel contains detail of the state of a Mie inversion after the first minimization up to 2000 cm^{-1}. The solid line shows the experimental aerosol spectrum while the dotted line represents the results of the Mie calculation. The lower panel shows the difference between the two spectra. Note the good agreement between the two at this point in the inversion. The minor discrepancies displayed here more than likely come from the estimated k used to start the inversion. The ensuing corrections will minimize the difference between the two spectra.

where $\langle C_{\mathrm{ext}}\rangle$ is the average extinction cross-section, Q_{ext} is the particle extinction efficiency, and Δr is the log-normal distribution step size, which was set to 0.04 μm in this study; the average scattering cross-section, $\langle C_{\mathrm{sca}}\rangle$, is obtained by substituting the particle scattering efficiency, Q_{sca}, for Q_{ext} in this equation. The bounds of the summation were chosen to include 99.7% of all particle radii in the distribution. Equation 9 was evaluated at every data point between 750 and 5000 cm^{-1}; the experimental points between 700 and 750 cm^{-1} were not included in the Mie calculation due to their use in extending the frequency range of the scalable k spectrum discussed above.

3.5. Comparison of Spectra, Iteration, and Corrections to *k*. The average extinction cross-sections need to be properly scaled in order to compare the computed Mie and observed aerosol extinction spectra. This is accomplished by first calculating an internal scaling factor, $N = E(\tilde{\nu}_N)/\langle C_{\mathrm{ext}}(\tilde{\nu}_N)\rangle$, at a frequency $\tilde{\nu}_N$ far from any region in the spectrum that contains absorption bands, which in this study was chosen to be 3500 cm^{-1}. The scaling factor represents the product of the particle number density and the path length through the aerosol, both of which are not directly measured in this study, and is used in the calculation of the sum of the squares of the discrepancies between the computed and observed spectra, $\chi^2 = \sum (\Delta E(\tilde{\nu}))^2$, where $\Delta E(\tilde{\nu}) = E(\tilde{\nu}) - N\langle C_{\mathrm{ext}}(\tilde{\nu})\rangle$ and the sum is carried out over all experimental frequencies between 750 and 5000 cm^{-1}. Brent's iterative nonlinear least-squares procedure PRAXIS[61] is used to minimize χ^2 through the variation of parameters r_g, σ_g, and κ.

As Clapp et al.[32] observed in their work, there is good overall agreement here between the computed and observed carvone aerosol spectra after χ^2 has been minimized, but small discrepancies do exist between them on a local band level, an example of which is shown in Figure 9. The fact that ΔE is not necessarily equal to zero at each experimental frequency can be due to uncertainties in the optical constants or the true character of the particle size distribution. Neglecting the latter for now, the former is undoubtedly related to our assumption that the imaginary component of the complex refractive index is linearly proportional to $E/\tilde{\nu}$ from the nonscattering thin-film extinction spectrum. To eliminate these small discrepancies, we employ a technique to correct k in a manner that is analogous to the method used by Hawranek et al. to compensate for dispersion-related distortions in their thin-film studies.[47]

The discrepancy calculated above, ΔE, can be written as the sum of two components, ΔE_{abs} and ΔE_{sca}, which correspond to discrepancies in the absorption and scattering components of the spectra. The absorption component may be written as $\Delta E_{\mathrm{abs}} = N\Delta\langle C_{\mathrm{abs}}\rangle = N\Delta\alpha_{\mathrm{abs}}\langle V\rangle$, where $\langle C_{\mathrm{abs}}\rangle$ and $\langle V\rangle$ respectively represent the average absorption cross-section and volume of the particles. Substituting eq 5 into this expression along with $\langle V\rangle = 4\pi\langle r^3\rangle/3$, where $\langle r^3\rangle$ is the average cubic radius of the particles, yields, upon rearrangement,

$$\Delta k(\tilde{\nu}) = \frac{\Delta E_{\mathrm{abs}}(\tilde{\nu})}{16\pi^2 N\tilde{\nu}\langle r^3\rangle/3} \tag{10}$$

which relates discrepancies in the absorption component of the aerosol extinction to Δk, a discrepancy in the imaginary part of the complex refractive index at each frequency. Although the value of ΔE_{abs} cannot be directly determined, it can be estimated from results of the Mie scattering calculations. Using the relationship between the absorption and scattering components of extinction, ΔE_{abs} may be written as

$$\Delta E_{\mathrm{abs}}(\tilde{\nu}) = \Delta E(\tilde{\nu})\left(1 - \frac{\Delta E_{\mathrm{sca}}(\tilde{\nu})}{\Delta E(\tilde{\nu})}\right) = \Delta E(\tilde{\nu})\left(1 - \frac{(N\Delta\langle C_{\mathrm{sca}}(\tilde{\nu})\rangle)}{(N\Delta\langle C_{\mathrm{ext}}(\tilde{\nu})\rangle)}\right) \tag{11}$$

Assuming that the ratio of scattering to extinction is the same for both ΔE and E, the term $(N\Delta\langle C_{\mathrm{sca}}\rangle)/(N\Delta\langle C_{\mathrm{ext}}\rangle)$ in eq 11 can be replaced with $\langle C_{\mathrm{sca}}\rangle/\langle C_{\mathrm{ext}}\rangle$. Defining Δk as $k^{(l+1)} - k^{(l)}$ where $k^{(l+1)}$ is the set of corrected imaginary components to use in the next minimization and $k^{(l)}$ is the set of imaginary components obtained in the current minimization, and substituting eq 11 into eq 10, provides a means to generate a corrected set of imaginary components at the end of a PRAXIS minimization via

$$k(\tilde{\nu})^{(l+1)} = k(\tilde{\nu})^{(l)} + \frac{\Delta E(\tilde{\nu})[1 - (\langle C_{\mathrm{sca}}(\tilde{\nu})\rangle/\langle C_{\mathrm{ext}}(\tilde{\nu})\rangle)]}{16\pi^2 N\tilde{\nu}\langle r^3\rangle/3} \tag{12}$$

In this study, the correction procedure was automatically applied as long as χ^2 continued to decrease by more than 0.05% relative to its value at the end of the previous minimization.

4. Results and Discussion

Six spectra, shown in Figure 10, were chosen from several different experimental runs and subjected to the Mie inversion procedure described above. The inversion for each spectrum was initiated with the scaling factor κ set equal to 0.40 and values of r_g and σ_g as shown in Table 1. All entries in this table are unitless, except for the geometric mean radii which are given in units of microns (μm). The initial fit parameter values were not chosen randomly, but primarily based on our experience in analyzing other aerosol extinction spectra. Table 1 also lists the final values of the three fit parameters in addition to the number of minimizations needed to achieve convergence. All six refractive index data sets were then averaged to produce the final set of data shown in Figures 11 and 12 along with the SKO[27] optical constants, which were digitized directly from the

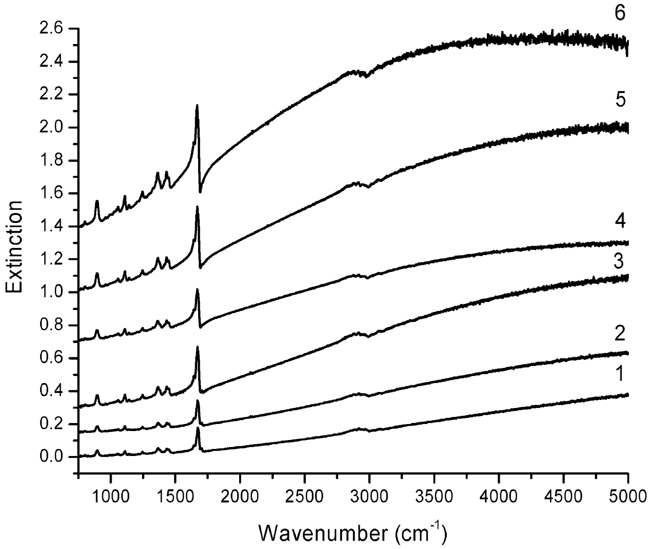

Figure 10. Six aerosol extinction spectra used in this study. The spectra were selected out of groups from several different experimental runs and are offset here for clarity. As mentioned in the text, we were careful to select spectra that showed evidence of both absorption and scattering. Scattering of light by the particles manifests itself as a sloping baseline on top of which the absorption bands are superimposed. The spectra labels correspond to the entries in Table 1.

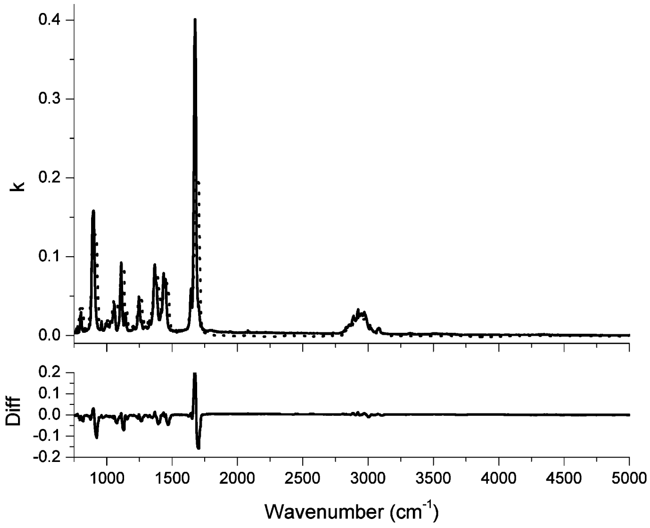

Figure 11. The top panel shows the imaginary component spectrum. The solid line represents the present imaginary components while the dotted line shows the digitized SKO[27] data set. The lower panel shows the difference between the two sets.

TABLE 1: Initial Fit Parameters and Mie Inversion Results (i = initial value)

	r_g^i	σ_g^i	r_g	σ_g	κ	l
1	0.30	1.8	0.298	1.85	0.430	1
2	0.90	1.3	0.927	1.26	0.383	14
3	0.90	1.4	0.928	1.36	0.405	21
4	0.95	1.4	0.898	1.48	0.398	11
5	0.97	1.4	0.934	1.45	0.386	11
6	1.20	1.4	1.221	1.40	0.415	8

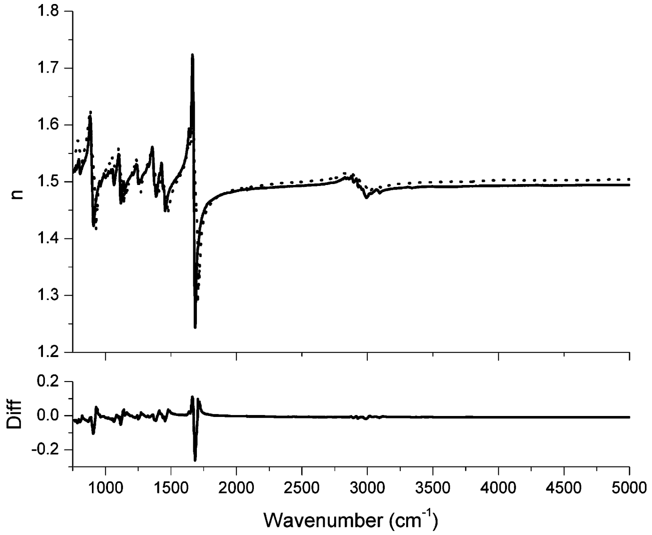

Figure 12. The top panel shows the real component spectrum. The solid line represents the present real components while the dotted line shows the digitized SKO[27] data set. The lower panel shows the difference between the two sets.

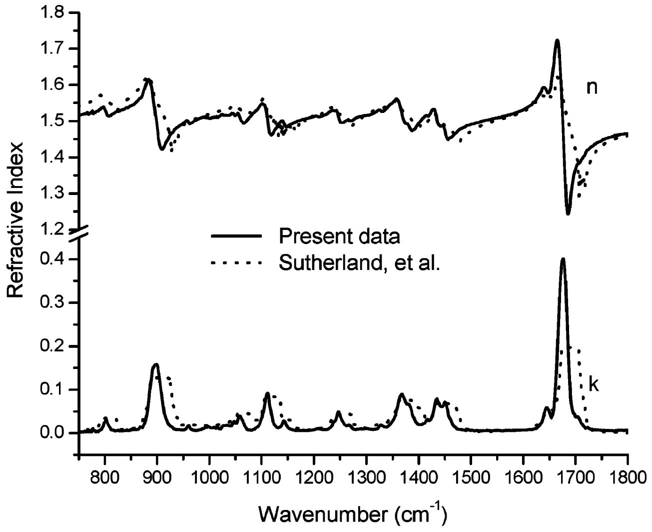

Figure 13. A detailed view of the discrepancies between the present optical constants and the SKO[27] data set. While there is general agreement between the band positions in these spectra, there are differences in certain bandwidths and heights.

literature as their data set is no longer available in tabulated form.[41] The complete set of complex refractive index data is available through the journal as Supporting Information.

In general, there is good qualitative agreement between the band positions within the two sets of refractive indices. As shown in Figure 13, there are some differences in the width and height of certain bands, some of which are undoubtedly due to the digitization of the poorly resolved literature plots. Nevertheless, the fact that the ordinate axis for the SKO imaginary component spectrum ranges from zero to 0.2 indicates that *k* apparently does not exceed 0.2 in the SKO data set.[27] In the present case, the largest imaginary component we retrieved was 0.401, which occurred at the peak of the intense carbonyl stretching band centered on 1677 cm^{-1} and is a factor of 2 times greater than the corresponding SKO value. Digitization certainly cannot solely account for the magnitude of this discrepancy. Although the original SKO axis could be mislabeled, the fact that the amplitude of the SKO real component data in this frequency region is smaller than that of the present results is consistent with their smaller *k* values. Deviations between refractive index data sets for a given material such as those observed here are commonplace, and their existence can often be traced back to procedural details.[62] It is tempting to cite instrumental resolution as a potential source of the discrepancies in the shape of this band and others, but in this case, both studies were performed with a resolution of 2 cm^{-1}. Unfortunately, the

TABLE 2: Fit Parameters and Mie Inversion Results for Uniqueness Test (i = initial value)

	r_g^i	σ_g^i	κ^i	r_g	σ_g	κ	N	χ^2	l
6	1.20	1.4	0.4	1.221096	1.401762	0.415212	0.05929	0.484587	8
6a	0.40	1.2	0.4	1.220857	1.401829	0.415557	0.05934	0.484271	8
6b	2.00	1.2	0.4	1.220773	1.401867	0.415040	0.05938	0.484288	8
6c	0.70	1.8	0.4	1.221447	1.401657	0.416523	0.05926	0.484416	8
6d	2.00	2.0	0.4	1.221289	1.401703	0.414919	0.05931	0.484190	8
6e	1.25	1.5	0.2	1.221142	1.401745	0.415609	0.05935	0.484283	8
6f	1.25	1.5	0.8	1.222003	1.401494	0.415174	0.05929	0.484463	8

lack of a complete quantitative SKO data set prohibits a full exploration of this topic at this time.

One concern in using an adjustable log-normal particle size distribution within the Mie inversion procedure is that of uniqueness, i.e., does the procedure find a single set of fit parameters for the lowest sum of the squares of the deviations between the computed and observed aerosol extinction spectra, or do multiple parameter sets exist, all with the same χ^2? In their work on nitric acid dehydrate (NAD) crystallization, Disselkamp et al. [63] observed that it was possible to fit an experimental extinction spectrum of NAD with two Mie-simulated spectra that were each computed for two different log-normal size distributions. Similar observations were made by Bertram and Sloan[64] in their study of NAD nucleation. Nonuniqueness in the current inversion procedure would obviously not be welcome, for it would lead to the retrieval of multiple valid sets of refractive index data. To avoid this issue, we took care to select only those aerosol spectra that showed signs of simultaneous absorption and scattering throughout the entire frequency range, as had been done in previous studies.[32,34,35] Such spectra contain features that are dependent on the fine interplay between the optical constants and the particle size distribution, and thus lead to unique solutions. To examine the topic of uniqueness in our case, we purposely distorted the initial fit parameters for some of our spectra to see if the retrieval procedure would converge to the same result in each case. Table 2 shows the initial fit parameters for the inversion of spectrum 6 in Figure 10. As in Table 1, the geometric mean radii are given in units of μm; the internal scaling factor N is given in units of μm^{-2}. Table 2 also lists the fit results to the sixth decimal position (except for N) to demonstrate the differences between the inversions. In each inversion, the current procedure yielded the same outcome to at least three significant figures, as should be the case when a unique solution is achieved.

One measure of the precision in the present data set is given by the uncertainty in the average value of κ, the imaginary component scaling factor. This is the only fit parameter of the three used in the inversion procedure that should not depend on the actual particle size since it is a gauge of the maximum value of k across the spectrum. In this case, the average κ was found to be 0.403 ± 0.007 ($\pm$ 2%). The absolute uncertainty in each value of k was found by computing the standard deviation of the mean, σ_k, from the six inversion results at each experimental frequency. As shown in the lower panel of Figure 14, the largest uncertainties in k occur in absorption band regions, but never exceed 0.011 refractive index units throughout the entire spectrum. Several sources of error contribute to the magnitude of σ_k, including uncertainties in the original thin-film and aerosol extinction spectra, but it is the noise in the latter that contributes the most through the correction of the imaginary components (eq 12).

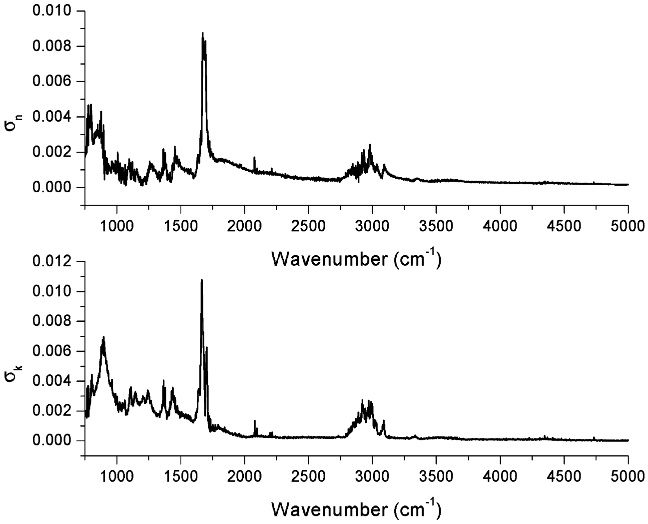

Figure 14. Plot of the absolute uncertainties in k and n. These data represent the standard deviation of the mean in k and n at each experimental frequency. The largest absolute uncertainties occur in the regions that contain absorption bands.

The absolute uncertainty in each of the real components, σ_n, was determined in the same manner and is shown in the upper panel of Figure 14. The frequency-dependent magnitude of σ_n is remarkably similar to that of σ_k, never exceeding 0.009 refractive index units across the spectrum. This behavior is predicted when the propagation of σ_k through $\Delta n(\tilde{\nu}_i)$, the second term on the right-hand side of eq 8, is considered. In this case, an estimate of the variance in $\Delta n(\tilde{\nu}_i)$ is given by

$$\sigma^2_{\Delta n(\tilde{\nu}_i)} = \left(\frac{2\Delta\tilde{\nu}}{\pi}\right)^2 \left\{ \sum_j{}' \left(\frac{1}{\tilde{\nu}_j - \tilde{\nu}_i}\right)^2 \sigma^2_{k(\tilde{\nu}_j)} + \sum_j{}' \left(\frac{1}{\tilde{\nu}_j + \tilde{\nu}_i}\right)^2 \sigma^2_{k(\tilde{\nu}_j)} \right\} \tag{13}$$

where i, j, and Σ' retain their previous definitions and the uncertainty in frequency is assumed to be negligible. Both sums in this equation contain the variance in $k(\tilde{\nu}_j)$ multiplied by the inverse square of either the difference or sum of $\tilde{\nu}_i$ and $\tilde{\nu}_j$. These terms serve as weighting factors that determine how much $\sigma^2_{k(\tilde{\nu}_j)}$ contributes to the overall variance in $\Delta n(\tilde{\nu}_i)$. The factors in the first sum are largest when $j = i \pm 1$ and quickly decrease for $j < i - 1$ and $j > i + 1$, while the factors in the second sum are always much smaller than those in the first for all values of j. Restricting the first sum in eq 13 to values of $j = i \pm 1$ and neglecting the contribution of the second sum yields

$$\sigma^2_{\Delta n(\tilde{\nu}_i)} \approx \left(\frac{2\Delta\tilde{\nu}}{\pi}\right)^2 \frac{\sigma^2_{k(\tilde{\nu}_{i-1})} + \sigma^2_{k(\tilde{\nu}_{i+1})}}{(\Delta\tilde{\nu})^2} \approx \frac{8}{\pi^2}\sigma^2_{k(\tilde{\nu}_i)} \tag{14}$$

where the far right-hand side of eq 14 was obtained by further assuming that $\sigma^2_{k(\tilde{\nu}_i)} \approx \sigma^2_{k(\tilde{\nu}_{i-1})} \approx \sigma^2_{k(\tilde{\nu}_{i+1})}$. This result is consistent with the uncertainties shown in Figure 14. There is, however, a lower limit to the uncertainty in n. Recall that the real component is determined in eq 8 by adding a constant, $n(\infty)$, to $\Delta n(\tilde{\nu}_i)$. Since $n(\infty)$ is not dependent on k, its effect on σ_n is not included in either eq 14 or Figure 14. Strictly speaking, the overall variance in $n(\tilde{\nu}_i)$ is given by $\sigma^2_{n(\tilde{\nu}_i)} \approx \sigma^2_{n(\infty)} + \sigma^2_{\Delta n(\tilde{\nu}_i)}$ where $\sigma_{n(\infty)}$ was determined to be $\pm$ 0.001 earlier in this work. This implies that under conditions in which $\sigma_{\Delta n(\tilde{\nu}_i)} \ll \sigma_{n(\infty)}$, as is the case at high wavenumber, σ_n must approach a limiting value of $\pm$ 0.001.

One way to check the accuracy of the present data set is to use the optical constants in a Mie scattering fit of other aerosol extinction spectra for carvone that were collected in the

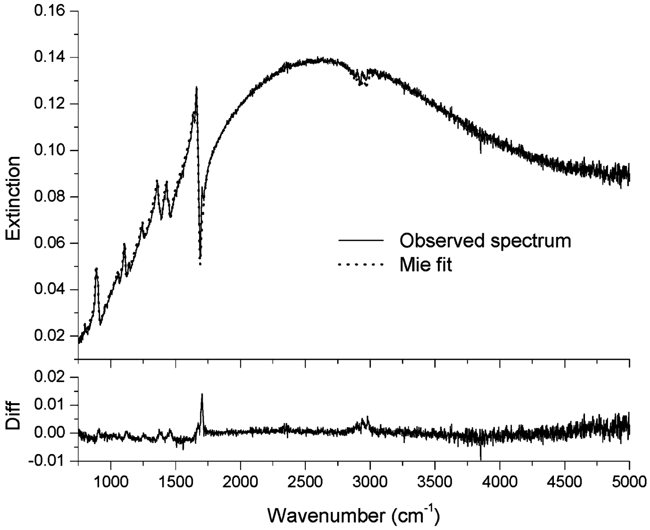

Figure 15. The top panel contains a Mie fit of an aerosol spectrum recorded in the laboratory. The fit is quite good as indicated by the difference spectrum in the lower panel. The fit reported a geometric mean radius of 2.24 μm and a geometric mean standard deviation of 1.25.

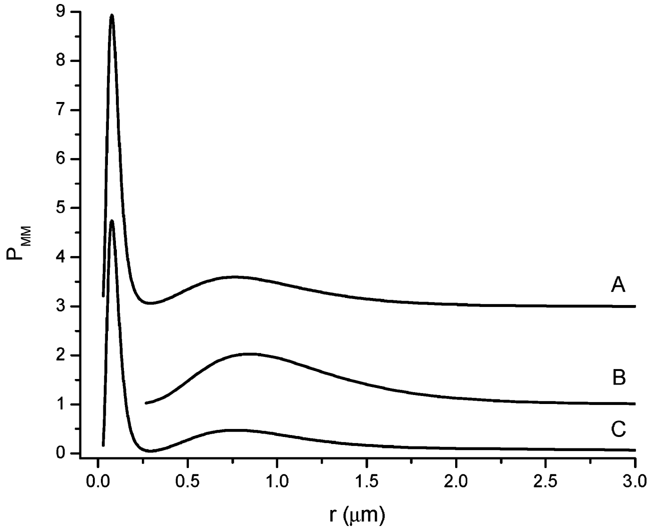

Figure 16. The multimodal particle size distributions used in generating the synthetic aerosol extinction spectra. The distribution plots have been offset for clarity.

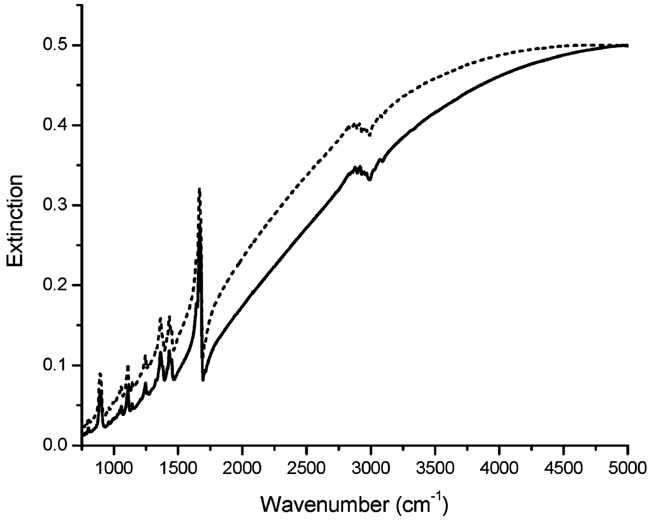

Figure 17. Two of the three synthetic aerosol extinction spectra listed in Table 3. The solid line represents the spectrum for test case A while the dashed line shows that of test case B. The subtle shift in the sloping baseline is due to changes in scattering as the size of the particles increases. The inversion of each spectrum resulted in an optical constant data set that is in agreement with the present results.

TABLE 3: Particle Size Distribution Parameters and Synthetic Mie Inversion Results (i = units of microns)

	w_1	w_2	w_3	$r^i_{g_2}$	$r^i_{g_3}$	r^i_g	σ_g	κ	χ^2	l
A	0.5	0.5	–	0.09	–	0.89	1.51	0.401	0.0008	12
B	0.5	0.5	–	1.13	–	0.98	1.55	0.403	0.0026	9
C	0.4	0.4	0.2	0.09	2.7	1.84	1.77	0.338	0.6275	1

laboratory but not used in the inversion procedure. As in the inversion procedure, the size distribution of the particles was not measured. Instead, the particle radii were assumed to be log-normally distributed according to eq 3, with r_g and σ_g serving as variable parameters in the nonlinear least-squares fitting procedure. An example of one of these Mie fits is displayed in Figure 15. In this case, the spectrum shows a strong scattering component with lobe-like structure that peaks near 2600 cm^{-1}, which suggests not only the presence of large particles but also a rather narrow size distribution since the lobe has a well-defined, finite width. Indeed, the fit reported a geometric mean radius and standard deviation of 2.24 μm and 1.25, respectively. The difference plot of Figure 15 shows little deviation between the observed and computed spectra across the frequency range and indicate that the optical constants presented here are appropriate for carvone.

The Mie fit shown in Figure 15 indicates that the optical constants reported here are consistent with our carvone aerosol spectra under conditions in which the particle radii are assumed to be log-normally distributed. As mentioned previously, log-normal assumptions are often used to describe the particle size distribution of single-source aerosols,[65] and are regularly made in a variety of applications including remote sensing retrievals,[66,67] climate modeling,[68,69] backscatter calculations,[70] and the simulation of bioaerosol spectral signatures.[71] There is, however, no particular reason why the size distribution of any aerosol should be log-normal. Indeed, several other types of functions have been employed to characterize particle size distributions, but they are often relegated to specific aerosol types.[65] To investigate how the inversion procedure described above might be affected by the use of extinction spectra for particles whose sizes are not log-normally distributed, we generated synthetic extinction spectra for several multimodal aerosol size distributions from the present optical constants and Mie theory, and then used these spectra as input to the inversion procedure. The multimodal size distributions were formed from the sum of weighted log-normal distributions

$$P_{\mathrm{MM}}(r) = \sum w_i P_{\mathrm{LN}}(r;r_{g_i},\sigma_{g_i}) \qquad (15)$$

where the w_i are weighting factors that properly normalize P_{MM} under the constraint $\sum w_i = 1$ and P_{LN} is given by eq 3; in general, sums of log-normal distributions are themselves not necessarily log-normal. The final optical constants and fit parameters for the synthetic spectra were then compared to the results reported above. Table 3 lists the parameters for three test distributions along with their corresponding inversion results. We arbitrarily set r_{g_1} to 0.90 μm and the σ_{g_i} to 1.50 in order to loosely correspond to the retrieved particle size parameters of spectra 2−5 in Table 1. Each of the multimodal distributions is shown in Figure 16 while the corresponding synthetic extinction spectra are shown in Figures 17 and 18.

Test case A represents an aerosol whose numbers are evenly

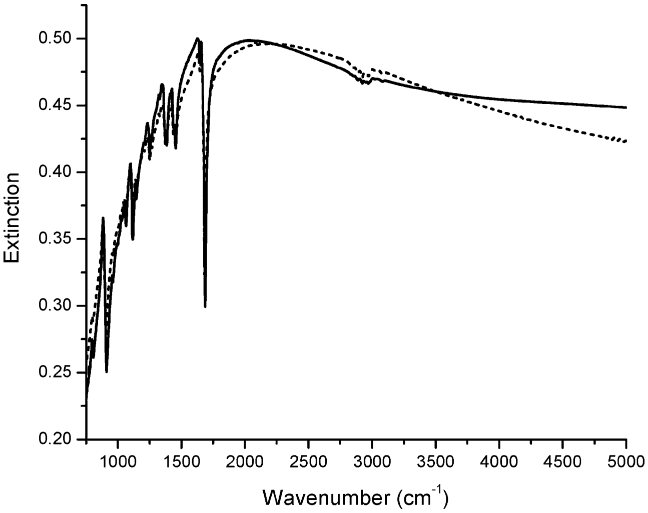

Figure 18. Mie inversion results for a trimodal particle size distribution. The solid line shows the synthetic spectrum for test case C in Table 3 while the dashed line shows the final state of the Mie inversion fit. The log-normal assumption used in the inversion procedure cannot account for the inclusion of larger sized particles, hence the poor agreement between the spectra.

divided between submicron- and micron-sized particles with geometric mean radii that differ by a factor of 10. In this case, the inversion of synthetic spectrum A yielded optical constants that are virtually indistinguishable from those reported above. Not only does the imaginary component scaling factor compare well with the average value of κ, but the average deviation in k and n over the entire frequency range is only 0.0003 refractive index units. The inversion also yielded an effective geometric mean radius and standard deviation that are consistent with r_{g_1} and σ_{g_1}, respectively. This result is not surprising. The smaller particles in the distribution contribute little to the absorption component of extinction since their volumes are approximately 3 orders of magnitude less than the larger particles. While the smaller particles do give rise to Rayleigh scattering, its magnitude is not significant in comparison to the Mie scattering brought about by the larger particles. The inversion procedure thus effectively sees only the spectral characteristics of the large particles in this distribution and proceeds accordingly.

Test case B also represents an aerosol that is evenly divided in number between two differently sized particles, but this time the geometric mean radii do not differ by that much. As in test case A, the inversion of synthetic spectrum B yielded optical constants and an imaginary component scaling factor that are in good agreement with the present data set. One particularly interesting feature about this particular bimodal distribution, however, is that it is pseudo-log-normal, i.e., the bimodal distribution can be characterized by a single geometric mean radius and standard deviation which in this case happen to be 1.01 μm and 1.52, respectively. As expected, the inversion of the synthetic spectrum determined log-normal parameters (see Table 3) that are consistent with the character of the pseudo-log-normal distribution. In cases like this, therefore, the log-normal assumption in the inversion procedure is expected to have no effect on the final results.

Upon a quick inspection of Figure 16, there does not appear to be much of a difference between the bimodal distribution of test case A and the trimodal distribution used in test case C. The additional component in the latter distribution, however, has a profound impact on the synthetic extinction spectra as displayed in Figure 18 where the fractional increase in the number of particles with radii exceeding 0.90 μm clearly affects the character of the spectrum. The inversion results for synthetic spectrum C are certainly not as good as in the previous test cases. The imaginary component scaling factor is nearly 20% lower than the average value of κ reported above, which implies that the imaginary components will be lower by a similar amount throughout the entire spectrum. This will also be true for the amplitude of the real components that are obtained from the imaginary components through the KK relationship.

Figure 18 and the χ^2 entry in Table 3 indicate that the inversion fit to synthetic spectrum C is poor. Indeed, the discrepancies between the synthetic spectrum and the fit become progressively worse at high wavenumber. The lack of a good fit to spectrum C is a direct result of the log-normal assumption. In this case the log-normal distribution function is simply incapable of including enough large particles to account for all of the absorption and scattering components in the extinction spectrum. The only way to improve the quality of the inversion fit under the log-normal assumption is to alter the optical constants themselves through the correction procedure of eq 12. Strictly speaking, this procedure operates only on the imaginary components in an attempt to correct minor fit discrepancies that arise from the initial guess of the imaginary component spectrum. It is not meant to compensate for the fact that the extinction spectrum undergoing inversion might be for an ensemble of particles whose radii are not log-normally distributed as in test case C. The number of minimizations (column l in Table 3) shows what happens when eq 12 is incorrectly applied. While test cases A and B go through several minimizations before the inversion procedure converges to a final set of optical constant data, the inversion of spectrum C stops after the first minimization due to the fact that χ^2 increases after the imaginary component correction is carried out. Attempts to use extinction spectra for aerosols distributed in a manner similar to test case C where the particle radii are perhaps spread out over several microns are likely to yield similar inversion results, thus making them relatively easy to identify and treat as suspect. None of the six extinction spectra used in the inversion procedure above exhibited this behavior, thus making it likely that the aerosol radii were, or could be characterized as, log-normally distributed.

The complete set of complex refractive index data for carvone is available from the authors upon request. The optical constants are also available online in a tab separated ASCII file at http://chemistry.che.depaul.edu/rniedzie.

5. Summary

Here we report the frequency-dependent complex refractive indices of carvone obtained from the Mie inversion of aerosol extinction spectra recorded at room temperature. The optical constants are in good qualitative agreement with those measured by Sutherland et al.,[27] however, there appear to be deviations of up to a factor of 2 in some bands. A full quantitative analysis of these deviations cannot be performed at this time since the SKO refractive indices are no longer available in tabulated form.[41] The largest absolute uncertainties in the imaginary components of the present data set are largest in the band regions but never exceed 0.011 refractive index units. The largest uncertainties in the real components likewise occur in band regions, but never exceed 0.009 refractive index units. The complex refractive indices have been used here to successfully model other carvone aerosol spectra recorded in our laboratory. They also add to the small number of other optical constant data sets for organic systems that are available for use in modeling applications and the interpretation of remote sensing measurements.

Acknowledgment. We gratefully acknowledge The Research Corporation (Cottrell College Science Award CC5399) and the College of Liberal Arts and Sciences of DePaul University (Faculty Summer Research and Development Grant and Undergraduate Research Assistant Program) for their support of this project. We also thank E. M. Lucchetta for her help in the early stages of this experiment.

Supporting Information Available: The entire optical constant data set for carvone. This material is available free of charge via the Internet at http://pubs.acs.org.

References and Notes

(1) Schwartz, S. E.; Andreae, M. O. *Science* **1996**, *272*, 1121.

(2) Jonas P. R.; Charlson, R. J.; Rodhe, H. *Climate Change 1994: Radiative Forcing of Climate Change and An Evaluation of the IPCC 1S92 Emission Scenarios*; Cambridge University Press: Cambridge, 1995; Chapter 3, pp 127−165.

(3) Lacis A. A.; Mishchenko, M. I. *Aerosol Forcing of Climate*; John Wiley & Sons: New York, 1995; pp 11−42.

(4) Rogge, W. F.; Mazurek, M. A.; Hildemann, L. M.; Cass, G. R.; Simoneit, B. R. T. *Atmos. Environ.* **1993**, *27A*, 1309.

(5) Husar, R. B.; Holloway, J. M.; Patterson, D. E.; Wilson, W. E. *Atmos. Environ.* **1981**, *15*, 1919.

(6) Marti, J. J.; Weber, J. R.; McMurry, P. H.; Eisele, F.; Tanner, D.; Jefferson, A. *J. Geophys. Res.* **1997**, *102*, 6331.

(7) Simoneit, B. R. T. *J. Atmos. Chem.* **1989**, *8*, 251.

(8) Simoneit, B. R. T.; Mazurek, M. A. *Atmos. Environ.* **1992**, *16*, 2139.

(9) Monahan E. C. *The Role of Air-Sea Exchange in Geochemical Cycling*; D. Reidel: Dordrecht, 1986; pp 129−163.

(10) Bowman, F. M.; Odum, J. R.; Seinfeld, J. H. *Atmos. Environ.* **1997**, *31*, 3921.

(11) Odum, J. R.; Jungcamp, T. P. W.; Griffin, R. J.; Forstner, H. J. L.; Flagan, R. C.; Seinfeld, J. H. *Environ. Sci. Technol.* **1997**, *31*, 1890.

(12) Grosjean, D.; Williams, E. L., II; Grosjean, E.; Novakov, T. *Aerosol Sci. Technol.* **1994**, *21*, 306.

(13) Charlson, R. J.; Heintzenberg, J. *Aerosol Forcing of Climate*; John Wiley & Sons: New York, 1995; pp 1−10.

(14) Pueschel R. F. *Aerosol Effects on Climate*, 1st ed.; The University of Arizona Press: Tucson, 1993; Chapter 3, pp 110−132.

(15) Schwartz S. E. *Aerosol Forcing of Climate*; John Wiley & Sons: New York, 1995; pp 251−280.

(16) Lund Myhre, C. E.; Christensen, D. H.; Nicolaisen, F. M.; Nielsen, C. J. *J. Phys. Chem. A* **2003**, *107*, 1979.

(17) Bohren, C. F.; Huffman, D. R. *Absorption and Scattering of Light by Small Particles*, 1st ed.; John Wiley & Sons: New York, 1983.

(18) Kerker, M. *The Scattering of Light and Other Electromagnetic Radiation*, 1st ed.; Academic Press: New York, 1969.

(19) van de Hulst, H. C. *Light Scattering by Small Particles*, 2nd ed.; Dover Publications: New York, 1981.

(20) Bertie, J. E.; Jones, R. N.; Keefe, C. D. *Appl. Spectrosc.* **1993**, *47*, 891.

(21) Hawranek, J. P.; Jones, R. N. *Spectrochim. Acta* **1976**, *32A*, 111.

(22) Bertie, J. E.; Jones, R. N.; Apelblat, Y. *Appl. Spectrosc.* **1994**, *48*, 144.

(23) Bertie, J. E.; Jones, R. N.; Apelblat, Y.; Keefe, C. D. *Appl. Spectrosc.* **1994**, *48*, 127.

(24) Bertie, J. E.; Lan, Z.; Jones, R. N.; Apelblat, Y. *Appl. Spectrosc.* **1995**, *49*, 840.

(25) Bertie, J. E.; Zhang, S. L.; Eysel, H. H.; Baluja, S.; Ahmed, M. K. *Appl. Spectrosc.* **1993**, *47*, 1100.

(26) Sutherland, R. A.; Khanna, R. K. *Aerosol Sci. Technol.* **1991**, *14*, 331.

(27) Sutherland, R. A.; Khanna, R. K.; Ospina, M. J. *Aerosol Sci. Technol.* **1994**, *20*, 62.

(28) Signorell, R.; Luckhaus, D. *J. Phys. Chem. A* **2002**, *106*, 4855.

(29) Toon, O. B.; Pollack, J. B.; Khare, B. N. *J. Geophys. Res.* **1976**, *81*, 5733.

(30) Ackerman, T. P.; Toon, O. B. *Appl. Opt.* **1981**, *20*, 3661.

(31) Gillespie, J. B.; Jennings, S. G.; Lindberg, J. D. *Appl. Opt.* **1978**, *17*, 991.

(32) Clapp, M. L.; Miller, R. E.; Worsnop, D. R. *J. Phys. Chem.* **1995**, *99*, 6317.

(33) Richwine, L. J.; Clapp, M. L.; Miller, R. E.; Worsnop, D. R. *Geophys. Res. Lett.* **1995**, *22*, 2625.

(34) Niedziela, R. F.; Miller, R. E.; Worsnop, D. R. *J. Phys. Chem. A* **1998**, *102*, 6477.

(35) Niedziela, R. F.; Norman, M. L.; DeForest, C. L.; Miller, R. E.; Worsnop, D. R. *J. Phys. Chem. A* **1999**, *103*, 8030.

(36) Norman, M. L.; Qian, J.; Miller, R. E.; Worsnop, D. R. *J. Geophys. Res.* **1999**, *104*, 30571.

(37) Heathfield, A. E.; Newnham, D. A.; Ballard, J.; Grainger, R. G.; Lambert, A. *Appl. Opt.* **1999**, *38*, 6408.

(38) Simonsen, J. L. *The Terpenes*, 2nd ed.; Cambridge University Press: Cambridge, 1947.

(39) Whittaker D. *Chemistry of Terpenes and Terpenoids*; 1st ed.; Academic Press: London, 1972; Chapter 2, pp 11−87.

(40) Chen, X.; Simoneit, B. R. T. *J. Atmos. Chem.* **1994**, *18*, 17.

(41) Sutherland, R. A., personal communication, 2001.

(42) Lovejoy, E. R.; Huey, L. G.; Hanson, D. R. *J. Geophys. Res.* **1995**, *100*, 775.

(43) Richardson, R. L., Jr.; Yang, H.; Griffiths, P. R. *Appl. Spectrosc.* **1998**, *52*, 572.

(44) Dohm, M. T.; Niedziela, R. F., unpublished data, 2003.

(45) Milham, M. E.; Frickel, R. H.; Embury, J. F.; Anderson, D. H. *J. Opt. Soc. Am.* **1981**, *71*, 1099.

(46) Fuchs, N. A. *The Mechanics of Aerosols*, 1st ed.; Dover Publications: Mineola, NY, 1989.

(47) Hawranek, J. P.; Neelakantan, P.; Young, R. P.; Jones, R. N. *Spectrochim. Acta* **1976**, *32A*, 85.

(48) Nefedov, A. P.; Petrov, O. F.; Vaulina, O. S. *Appl. Opt.* **1997**, *36*, 1357.

(49) Jones, M. R.; Curry, B. P.; Brewster, M. Q.; Leong, K. H. *Appl. Opt.* **1994**, *33*, 4025.

(50) Ahrenkiel, R. K. *J. Opt. Soc. Am.* **1971**, *61*, 1651.

(51) Hawranek, J. P.; Jones, R. N. *Spectrochim. Acta* **1976**, *32A*, 99.

(52) Hawranek, J. P.; Neelakantan, P.; Young, R. P.; Jones, R. N. *Spectrochim. Acta* **1976**, *32A*, 75.

(53) Biermann, U. M.; Luo, B. P.; Peter, Th. *J. Phys. Chem. A* **2000**, *104*, 783.

(54) Tisdale, R. T.; Glandorf, D. L.; Tolbert, M. A.; Toon, O. B. *J. Geophys. Res. −Atmos.* **1998**, *103*, 25353.

(55) *The Aldrich Library of Infrared Spectra*, 3rd ed.; Aldrich Chemical Co.: Milwaukee, WI, 1981; p. 265.

(56) Press, W. H.; Teukolsky, S. A.; Vetterling, W. T.; Flannery, B. P. *Numerical Recipes in FORTRAN*, 2nd ed.; Cambridge University Press: Cambridge, 1992.

(57) Warren, S. G. *Appl. Opt.* **1984**, *23*, 1206.

(58) Ohta, K.; Ishida, H. *Appl. Spectrosc.* **1988**, *42*, 952.

(59) Bertie, J. E.; Lan, Z. *J. Chem. Phys.* **1995**, *103*, 10152.

(60) Bauer N.; Fajans, K.; Lewin, S. Z. *Technique of Organic Chemistry*, 3rd ed.; Interscience Publishers: New York, 1959; Chapter XVIII, pp 1139−1281.

(61) Brent, R. P. *Algorithms for Minimization Without Derivatives*, 2nd ed.; Dover Publications: Mineola, NY, 2002.

(62) Wagner, R.; Mangold, A.; Möhler, O.; Saathoff, H.; Schnaiter, M.; Schurath, U. *Atmos. Chem. Phys. Discuss.* **2003**, *3*, 2219.

(63) Disselkamp, R. S.; Anthony, S. E.; Prenni, A. J.; Onasch, T. B.; Tolbert, M. A. *J. Phys. Chem.* **1996**, *100*, 9127.

(64) Bertram, A. K.; Sloan, J. J. *J. Geophys. Res. −Atmos.* **1998**, *103*, 3553.

(65) Hinds, W. C. *Aerosol Technology*, 2nd ed.; Wiley: New York, 1999.

(66) Lee, K. M.; Park, J. H.; Kim, Y.; Choi, W.; Cho, H. K.; Massie, S. T.; Sasano, Y.; Yokota, T. *J. Geophys. Res. −Atmos.* **2003**, *108*, 4228.

(67) Oshchepkov, S.; Sasano, Y.; Yokota, T. *Appl. Opt.* **2002**, *41*, 4234.

(68) Lesins, G.; Chylek, P.; Lohmann, U. *J. Geophys. Res. −Atmos.* **2002**, *107*, 4094.

(69) Liao, H.; Adams, P. J.; Chung, S. H.; Seinfeld, J. H.; Mickley, L. J.; Jacob, D. J. *J. Geophys. Res. −Atmos.* **2003**, *108*, 4001.

(70) Jarzembski, M. A.; Norman, M. L.; Fuller, K. A.; Srivastava, V.; Cutten, D. R. *Appl. Opt.* **2003**, *42*, 922.

(71) Ligon, D. A.; Wetmore, A. E.; Gillespie, P. S. *Optics Express* **2002**, *10*, 909.